Nanoscale

PAPER

View Article Online
View Journal | View Issue

Cite this: *Nanoscale*, 2022, **14**, 12297

Mesoporous silica as a matrix for photocatalytic titanium dioxide nanoparticles: lipid membrane interactions†

Elisa Parra-Ortiz,‡[a] Lucrezia Caselli,[a] Monica Agnoletti,[a] Maximilian W. A. Skoda,[b] Xiaomin Li,[c] Dongyuan Zhao[c] and Martin Malmsten *[a,d]

In the present study, we investigate the combined interaction of mesoporous silica (SiO_2) and photocatalytic titanium dioxide (TiO_2) nanoparticles with lipid membranes, using neutron reflectometry (NR), cryo-transmission electron microscopy (cryo-TEM), fluorescence oxidation assays, dynamic light scattering (DLS), and ζ-potential measurements. Based on DLS, TiO_2 nanoparticles were found to display strongly improved colloidal stability at physiological pH of skin (pH 5.4) after incorporation into either smooth or spiky ("virus-like") mesoporous silica nanoparticles at low pH, the latter demonstrated by cryo-TEM. At the same time, such matrix-bound TiO_2 nanoparticles retain their ability to destabilize anionic bacteria-mimicking lipid membranes under UV-illumination. Quenching experiments indicated both hydroxyl and superoxide radicals to contribute to this, while NR showed that free TiO_2 nanoparticles and TiO_2 loaded into mesoporous silica nanoparticles induced comparable effects on supported lipid membranes, including membrane thinning, lipid removal, and formation of a partially disordered outer membrane leaflet. By comparing effects for smooth and virus-like mesoporous nanoparticles as matrices for TiO_2 nanoparticles, the interplay between photocatalytic and direct membrane binding effects were elucidated. Taken together, the study outlines how photocatalytic nanoparticles can be readily incorporated into mesoporous silica nanoparticles for increased colloidal stability and yet retain most of their capacity for photocatalytic destabilization of lipid membranes, and with maintained mechanisms for oxidative membrane destabilization. As such, the study provides new mechanistic information to the widely employed, but poorly understood, practice of loading photocatalytic nanomaterials onto/into matrix materials for increased performance.

Received 8th April 2022,
Accepted 14th July 2022

DOI: 10.1039/d2nr01958b

rsc.li/nanoscale

Introduction

Novel strategies are urgently needed to address resistance development among bacteria against conventional antibiotics.[1] Inorganic nanoparticles are attracting considerable current interest in this context, as they can be triggered by various stimuli, and also offer opportunities for combination therapies with antimicrobial peptides and other antimicrobial compounds for new and synergistic properties.[2,3] Of particular interest to the present investigation, photocatalytic nanoparticles are strongly antimicrobial upon irradiation. This is due to the generation of highly reactive oxygen species (ROS), which in turn destabilize bacterial membrane components, such as phospholipids and lipopolysaccharides. Both direct binding and membrane interactions have been suggested to be important for such effects, but the relative importance of nanoparticle-mediated membrane destabilization and oxidative degradation of membrane lipids and other key bacterial components remains unclear.[4–6]

[a]*Department of Pharmacy, University of Copenhagen, DK-2100 Copenhagen, Denmark. E-mail: martin.malmsten@sund.ku.dk*
[b]*ISIS Pulsed Neutron and Muon Source, Rutherford Appleton Laboratory, OX11 0QX Harwell, Oxfordshire, UK*
[c]*Department of Chemistry, Collaborative Innovation Center of Chemistry for Energy Materials, State Key Laboratory of Molecular Engineering of Polymers, Fudan University, 200433 Shanghai, P. R. China*
[d]*Department of Physical Chemistry 1, University of Lund, SE-22100 Lund, Sweden*

†Electronic supplementary information (ESI) available: Calculated SLDs, summaries of structural data obtained from neutron reflectometry experiments, neutron reflectivity curves and best fits, effective particle size distributions from dynamic light scattering, cryoTEM images of TiO_2 nanoparticles, as well as data on oxidation kinetics. A schematic illustration of the model used, input parameters used for NR fits, and structural parameters obtained from NR fits. See DOI: https://doi.org/10.1039/d2nr01958b

‡Present address: Dep. Application Systems Analysis, Division of Protein Chemistry and Assays, Novozymes, Biologiens Vej 2, DK-2800 Kgs. Lyngby (Denmark).

Various photocatalytic nanoparticles, such as TiO_2, quantum dots, metal nanoparticles, and a range of carbon-based nanomaterials (fullerene, carbon nanorods, graphene, and graphitic carbon nitrides), as well as their heterojunction combinations, have been found to display potent antimicrobial properties.[4] Among these, the present study focuses on TiO_2 nanoparticles. While the wide band gap of such nanoparticles (3.2 eV (ref. 7)) requires triggering by UV and causes limitations in applications due to the short penetration depth of the latter, the need for UV triggering is an advantage in mechanistic studies on the interplay between direct membrane interactions and oxidative degradation triggered upon illumination. Thus, baseline ('in darkness') studies can be performed under regular laboratory light, thereby obtaining information of direct particle-membrane interactions in the absence of oxidative stress. By turning on UV illumination, ROS formation and oxidative destabilization of the lipid membranes is triggered and can be conveniently monitored.

A known challenge with the use of photocatalytic nanoparticles in biological systems is that of insufficient colloidal stability. While approaches for surface modification to induce electrostatic or steric stability of such nanoparticles have been attempted,[8,9] these come with another complications, since such surface modification may prevent photogenerated electrons and holes to reach the surface of the nanoparticles and react with water and dissolved oxygen, a pre-requisite for ROS formation.[10] As an alternative approach, photocatalytic nanoparticles may be incorporated into other nanomaterials and/or matrices for colloidal stability.[11,12] While the latter type of systems have been found to display advantageous photocatalytic effects, key factors affecting this have not been explored so far. Thus, there is very little knowledge on: (i) the interplay between direct membrane interactions and photocatalytic effects of such hybrid nanomaterials, and (ii) how photocatalytic nanoparticle loading to the matrix particles/materials affect their susceptibility to light triggering, as well as subsequent ROS generation within the matrix material, ROS diffusion through the matrix to reach the lipid membranes, and oxidative destabilization of the latter. Addressing all these aspects is the aim of the present investigation.

We here employ mesoporous silica nanoparticles as matrices into which we load TiO_2. The former are interesting delivery systems due to the well-defined pores in the nm range, allowing precise drug release through control of their surface area, as well as pore size, form, and composition. In addition, their negatively charged surface allows direct loading of cationic molecules or nanoparticles.[13] For such materials, we have previously addressed possibilities arising from the use of different morphologies, and demonstrated that virus-like silica nanoparticles, consisting of mesoporous cores (~100 nm size) coated by spiky nanotubes (~50 nm long, ~10 nm thick),[14] are able to effectively 'puncture' bacterial membrane mimicking bilayers and cause important structural changes.[15] By comparing such virus-like particles with corresponding smooth mesoporous silica nanoparticles of comparable core size and pore size as matrices for TiO_2 nanoparticles, novel insight can be obtained into the interplay between topology and oxidative stress for membrane destabilization. For this, lipid membrane interactions were compared between virus-like and smooth mesoporous silica nanoparticles of similar size (≈250 nm) surface charge (ζ-potential ≈−40 mV), and pore size (≈4–10 nm) loaded with TiO_2 nanoparticles (≈4–8 nm).

Previously, we investigated effects of UV-activated TiO_2 nanoparticles on different lipid membranes, including model mammalian cell (phosphatidylcholine (PC)/cholesterol) and bacterial (PC/phosphatidylglycerol (PG)) membranes.[16,17] It was observed that incorporation of anionic PG dramatically enhanced the susceptibility of these membranes to oxidative degradation, whereas cholesterol was found to have a stabilizing affect against oxidation.[17] Extending on this previous work, we set out in the present study to investigate the interaction of combined SiO_2/TiO_2 nanoparticles with previously employed PC/PG-based model lipid system, investigating supported lipid bilayers and large unilamellar vesicles using a set of complementary techniques, including neutron reflectometry (NR), cryogenic transition electron microscopy (cryo-TEM), fluorescence oxidation and leakage assays, dynamic light scattering (DLS), and ζ-potential measurements, for a comprehensive investigation of membrane interactions.

Materials and methods

Materials

TiO_2 nanoparticles (anatase, 4–8 nm) in aqueous suspension were obtained from PlasmaChem GmHb (Berlin, Germany). 1-Palmitoyl-2-oleoyl-*sn-glycero*-3-phosphocholine (16 : 0–18 : 1 PC, POPC), 1-palmitoyl-2-arachidonoyl-*sn*-phosphatidylcholine (16 : 0–22 : 4 PC, PAPC), and 1-palmitoyl-2-oleoyl-*sn-glycero*-3-phospho-(1′-*rac*-glycerol) (sodium salt) (16 : 0–18 : 1 PG, POPG), all of >99% purity, were from Avanti Polar Lipids (Alabaster, USA). C_{11}-BODIPY 581/591 was from Thermo Fisher Scientific (USA), while D-mannitol (>98%), superoxide dismutase bovine (SOD, bovine, recombinant, expressed in *E. coli*, ≥90%), Tris buffer (Trizma® base, ≥99.9%), acetic acid (99.7%), sodium acetate (≥99%), sodium chloride (>99.5%), D_2O (>99.9%), and all other chemicals and reagents were of analytical grade and obtained from Sigma Aldrich (St Luis, USA). Ultrapure Milli-Q water (MQ, 18.2 MΩ cm) was used for all experiments (Milli-Q Reference A+ Water Purification System, Merck KGaA, Darmstadt, Germany). With regards to inclusion of unsaturated PAPC, this was added to facilitate degradation at conditions where the UV lamp is at a good distance from the sample. The reason for this, in turn, is to avoid any heating of the sample, which may result in poorly controlled effects not related to ROS generation. Thus, the use of the unsaturated lipids is for experimental control purposes only, and *does not* imply that experiments cannot be done without them, or that the approaches taken cannot be translated to studies of bacteria.

Synthesis of mesoporous silica nanoparticles

Smooth and virus-like mesoporous silica nanoparticles were synthesised as described previously.[14] In short, for smooth mesoporous nanoparticles, 90 mg of triethanolamine and 1 g of hexadecyltrimethylammonium bromide (CTAB) were added to 20 mL of water. The solution was stirred at 60 °C for 1 h in flask. Then, a mixture of 1.5 mL of tetraethyl orthosilicate (TEOS) and 6 mL of cyclohexane were added and kept under stirring for 24 h. For virus-like mesoporous silica nanoparticles, 0.8 mL of NaOH (0.1 M) and 1 g of CTAB were added to 50 mL of water and kept under stirring at 60 °C for 2 h. Subsequently, 20 mL of TEOS in cyclohexane (20 v/v %) were added to the solution and stirred at 60 °C for 48 h. Following synthesis, both types of nanoparticles were washed repeatedly with water and ethanol, dispersed in acetone and refluxed for 12 h to remove CTAB. Afterwards, the samples were washed in ethanol and dried in vacuum at 45 °C for 8 h.

Preparation of TiO_2/mesoporous silica nanoparticle combinations

Concentrated stocks (5000 ppm) of mesoporous silica and TiO_2 nanoparticles were first prepared by dispersing the dry nanoparticle powder in MQ in ultrasonication bath (Elmasonic P30H, Elma GmbH, Germany; set at 37 Hz, 70% amplitude, pulse mode) for at least 45 min or until all powder was dispersed. Then, the nanoparticles were mixed at the desired ratios in the desired buffer (*i.e.*, 10 mM acetate buffer for pH 3.4; 10 mM sodium acetate for pH 5.4; or 10 mM Tris for pH 7.4) at a concentration 5 times higher than the final concentration desired for the experiments, using thorough mixing to maximize dispersion efficiency. As the TiO_2 nanoparticles have pronounced tendency for aggregation, they were added after thorough vortexing of the silica dispersions, and subsequently vortexed and bath sonicated for 45 min more (37 Hz, 70%, pulse mode) to facilitate a homogeneous distribution. These 5x nanoparticles samples were then diluted 5 times in different solutions depending on the final desired pH: in 10 mM acetate buffer for pH 3.4; in 10 mM sodium acetate for pH 5.4; or in 10 mM Tris for pH 7.4. Just before the experiments, further dispersion in ultrasonication bath for 10 min was carried out. To increase the colloidal stability of TiO_2/mesoporous silica particles combinations, nanoparticles were mixed in 10 mM acetate buffer at pH 3.4 at a concentration 5 times higher than the final concentration desired for the experiments, and bath sonicated for at least 45 min. These 5x nanoparticles samples were then diluted 5 times in the desired buffer for a final pH of 5.4 or 7.4. To further enhance the colloidal stability at pH 5.4 and 7.4, samples were subsequently centrifuged at 2000 rpm for 10 min to obtain a quantitative precipitation of free TiO_2 NPs aggregates. The supernatants were subsequently collected and bath sonicated for 10 min just before the experiments. With regards to the latter step, TiO_2 nanoparticles are not substantially eliminated by the short sonication. At loading conditions, the TiO_2 nanoparticles are strongly positively charged (+36 ± 2 mV), whereas the mesoporous silica ones are negatively charged (−15± 2 mV). Considering this, TiO_2 nanoparticles bind strongly and may potentially also become kinetically trapped, particularly if entering into the mesoporous matrix, and not able to detach also at pH 5.4, where the z-potential of the TiO_2 and the silica particles are +20 ± 2 and −27 ± 3 mV, respectively, hence displaying a considerable charge contrast. In relation to this, we also note that the finding of TiO_2 nanoparticles remaining bound to the silica particles also at pH 5.4 indicates that at least a fraction of the TiO_2 nanoparticles becomes internalized into the mesoporous silica particles.

Dry lipid film and liposome preparation

POPC, POPG and PAPC stocks (10 mg mL^{-1} in chloroform) were mixed at 50/25/25 molar ratio in dark glass vials under Ar atmosphere, followed by careful solvent evaporation, first by N_2 flow and then by 2 h in a vacuum desiccator. The dry lipid films were protected under Ar atmosphere and stored at −20 °C to prevent lipid oxidation. Just before liposome preparation, lipid films were thawed and hydrated at 22 °C in either buffer (for experiments with liposomes in suspension) or MQ (to prepare supported lipid bilayers) to the desired final concentration, using 8 cycles of 60 s bath sonication and 30 s vortexing to obtain multilamellar vesicles (MLVs). These MLVs were then used to prepare small unilamellar vesicles (SUV) for supported lipid bilayer formation. LUVs were prepared by 31 extrusion passes through 100 nm polycarbonate filters mounted in a LipoFast miniextruder (Avestin, Ottawa, Canada) at 22 °C. SUVs, in turn, were prepared by four 5 min cycles of tip sonication (UP50H, Hielscher Ultrasonics GmbH, Germany) in ice bath, with 2 min in between for cooling. None of these samples was degassed during hydration and preparation, thus dissolved O_2 is present in all hydrating and bathing media.

Size and ζ-potential measurements

Dynamic light scattering (DLS) was performed using a Zetasizer Nano ZSP (Malvern Pananalytical Ltd, Malvern, UK) to obtain average particles sizes and ζ-potentials. Measurements comprised 10 runs of 10 s, and were performed for both hydrodynamic size (173° back-scattering angle) and ζ-potential, with automatic attenuation and optical settings for all samples. Measurements were performed in triplicate at 25 °C. It should be noted here that inclusion of TiO_2 nanoparticles into the mesoporous silica matrices should influence the effective refractive index of the loaded composite nanoparticles. Quantitatively, however, these effects are minor, as evidenced by similar particle sizes obtained by DLS and cryoTEM at pH 3.4, in the absence of aggregation. Nevertheless, care should be taken not to overinterpret size distributions in particular. Furthermore, the translation from electrophoretic mobilities to ζ-potentials and further to charge densities is difficult for the virus-like nanoparticles due to the uncertainty of the location of the shear plane. In addition, surface structures effect local surface densities in a non-trivial

way. For example, at the same pH, ionic strength, and nanoparticle diameter, increasing the nanoparticle surface roughness has a direct effect on the local surface charge, being suppressed in "valleys" due to overlap of the electrical double layer, and enhanced on "peaks" by curvature effects.[18] In addition, the presence of the mesoporous pores may influence both hydrodynamic screening of the spikes and the extent of pinning of the flow lines at the interface, and hence also the translation of electrophoretic mobilities to effective ζ-potentials. Care should therefore be taken not to overinterpret the electrokinetic results, which should be used primarily to identify charge reversal pH and potential estimates.

Cryogenic transmission electron microscopy (cryo-TEM)

Cryo-TEM analyses were performed using a Tecnai G2 20 TWIN Transmission Electron Microscope (FEI, Hillsboro, OR, USA), operating at 80 kV in zero loss bright-field mode. To improve visualization, an underfocus of 1–2 μm was used. Samples were equilibrated at 25 °C for 1 h and prepared by using a FEI Vitrobot Mark IV. A small drop (~5 μl) of sample was deposited on a copper grid covered with a perforated polymer film and thin evaporated carbon layers. Excess liquid was removed by blotting with filter paper. Immediately after blotting, samples were vitrified in liquid ethane, held just above its freezing point. Samples were kept below −165 °C in a protected atmosphere during transfer and examination.

C_{11}-BODIPY 581/591 oxidation assays

The oxidation-sensitive and hydrophobic fluorescence probe C_{11}-BODIPY 581/591 was incorporated into POPC/POPG/PAPC bilayers (50/25/25 molar ratio) prepared in the different buffers. For this, 0.5 mol% of the probe was added to the organic solution prior to lipid film drying, always under Ar atmosphere. After hydration and extrusion, 0.5 mg mL^{-1} LUVs were subjected to *in situ* UV exposure in the presence or absence of 25 or 100 ppm TiO_2 nanoparticles, either free or loaded into 100 ppm of smooth or virus-like silica nanoparticles. Fluorescence spectra (λ_{ex} = 485 nm; λ_{em} = 500–700 nm) were acquired using a Cary Eclipse fluorescence spectrophotometer with Xe pulse lamp (Agilent Technologies, USA). The oxidation levels were quantified by monitoring the spectral shift of the probe emission from red (λ_{max} = 594 nm) to green (λ_{max} = 520 nm) and calculating the polarization index (PI):

$$\mathrm{PI} = \frac{I_{520} - I_{594}}{I_{520} + I_{594}} \quad (1)$$

Oxidation percentages were obtained by scaling the calculated PI values and fitting these for the first 5–10 min. These experiments were also performed in the presence of the D-mannitol ($^{\bullet}OH$ scavenger)[19] and SOD (superoxide inhibitor),[20] in order to pinpoint the effect of different ROS on lipid peroxidation and radical chain propagation in these bilayers. All measurements were performed in duplicate at 37 °C.

Neutron reflectometry (NR)

Structural features of supported POPC/POPG/PAPC bilayers (50/25/25 molar ratio) before, during, and after exposure to UV in the presence of TiO_2 nanoparticles, either free or loaded into smooth or virus-like silica nanoparticles, were characterized by NR following a previously established method.[15] Experiments were performed using the INTER reflectometer (ISIS Pulsed Neutron and Muon Source, Rutherford Appleton Laboratory, Harwell, UK.[21] Three incident angles (0.3°, 1.0° and 2.3°) were used to cover the whole Q-region of interest (~0.01 to 0.35 $Å^{-1}$). For kinetic measurements, the reflectometry changes at the first two angles were recorded every 10 min, acquiring data for 30 s at 0.3° and for 9 min 30 s at 1.0° in each 10 min cycle. Solid–liquid flow cells, the top plate of which was modified with a 30 mm diameter circular opening, were used together with UV-transparent quartz blocks (80 × 50 × 15 mm, 1 face polished, RMS < 4.5 Å, PI-KEM Ltd, Tamworth, UK) to allow *in situ* UV irradiation. The blocks were cleaned in dilute acid piranha solution (5/4/1 $H_2O/H_2SO_4/H_2O_2$) at 80 °C for 15 min, rinsed thoroughly in MQ, followed by 10 min of UV-ozone treatment (UV/Ozone ProCleaner, BioForce Nanosciences, USA). HPLC tubing, PEEK troughs, and O-rings were cleaned with 2% Hellmanex (Hellma Analytics, UK) in ultrasonication bath, then thoroughly rinsed and sonicated in MQ. A circulating water bath was used during the measurements to keep the sample cells at 37 °C.

The bare quartz surfaces were first characterized in D_2O and MQ. Then, they were pre-treated by rinsing 2 mM $CaCl_2$ into the cells, after which tip-probe sonicated SUV suspensions (0.1 mg mL^{-1}) were injected by syringe and allowed to deposit for 20 min. Subsequently, the excess was rinsed off with 10 mL MQ and 10 mL of the desired buffer at 2 mL min^{-1}. The bilayers thus formed were characterized in two contrasts, d- and h-buffer (10 mM Acetate/Tris buffer in MQ or in D_2O) before treatment. Contrasts were exchanged by pumping 20 mL of the desired buffer at 2 mL min^{-1}, and all buffers were degassed by bath sonication prior to experiments. Samples were then incubated for 10 min with 25 ppm TiO_2 nanoparticles, either free or loaded into 100 ppm of smooth or virus-like silica nanoparticles, in d-buffer at the desired pH. The bilayers were then subjected to *in situ* UV irradiation (Spectroline lamp ENF-260C, 6 W, 254 nm; 3 mW cm^{-2}) for 2 h. During this time, kinetic measurements were taken every 10 min. Immediately after UV exposure, the whole Q-range was measured in d-buffer, after which the bilayer was rinsed and characterized in both contrasts. The experimental NR profiles obtained in the different contrasts were fitted simultaneously by using the RasCAL reflectivity software.[22] A series of parallel layers (slabs) were used to model the interfacial structure, each of these described by a set of physical parameters, including thickness, roughness, hydration, and neutron scattering length density (SLD). The best fits of these parameters were then converted into SLD profiles, which represent the density distribution in the direction perpendicular to the reflecting interface. Fitting errors were estimated using Bootstrap algor-

ithms, considering random initial values for the input parameters included in the fits.[23] Experimental NR kinetics obtained in the d-buffer were fitted by using the Generic Optimization method the available on the Motofit software within the analysis package IGOR Pro. A similar multilayered structure was used to model the interface and obtain the SLD profiles,[24,25] while a Monte Carlo error analysis allowing for refitting data 200 times, was employed to minimize the uncertainty associated to data fitting.[26]

Results

TiO_2 loading into mesoporous silica nanoparticles

Effects of mixing TiO_2 and mesoporous SiO_2 nanoparticles were first investigated by DLS and ζ-potential measurements. As described in the Experimental section, the interpretation of ζ-potential values in these systems come with inherent challenges related to the presence of spikes for the virus-like particles (resulting in uncertainties of the position of the slip-plane and in curvature effects of the electric double layers), to the presence of pores in both the smooth and the virus-like SiO_2 nanoparticles (resulting in uncertainties of the location of the slip plane), and to compositional complexity due to the two-component nature of these systems. The ζ-potentials reported for the SiO_2 and TiO_2/SiO_2 systems should therefore be considered as effective values. With that in mind, the ζ-potential measurements of TiO_2 nanoparticles showed these to be positively charged (ζ-potential 36 ± 2 mV) at pH 3.4, less so (ζ-potential 20 ± 2 mV) at pH 5.4, and weakly negatively charged (ζ-potential −8 ± 2 mV) at pH 7.4 (Fig. 1A), in line with previously reported values of a point of zero charge (PZC) of pH ≈ 6–6.5.[27,28] In contrast, the smooth mesoporous silica nanoparticles were negatively charged (effective ζ-potential −15 ± 2 mV) already at pH 3.4, consistent with previously reported values of PZC of 1–2.[29] With increasing pH, the negative surface charge of these nanoparticles increased as a result of silanol group dissociation, reaching effective ζ-potentials of −27 ± 3 and −60 ± 2 mV at pH 5.4 and 7.4, respectively. For the virus-like nanoparticles, a weakly positive effective ζ-potential was observed at pH 3.4, an effect caused by the presence of the spikes, which complicates translation of electrophoretic mobilities to ζ-potentials due to both shear plane displacements and topological effects on the electrical double layer.[18] Also for the virus-like nanoparticles, an increasingly negative surface charge was observed with increasing pH (Fig. 1A). With the complexity of translating electrophoretic mobilities to ζ-potential values, colloidal stability needs to be ensured by another method, rather than inferred from ζ-potential results. Here, DLS was used for this purpose. As shown by particles size results obtained by DLS, TiO_2 nanoparticles were well dispersed at pH 3.4, but undergo pronounced aggregation at pH 5.4 and 7.4 (Fig. 1B and S1†), which was subsequently suppressed at higher pH.[16] Analogously, the virus-like mesoporous silica nanoparticles displayed some very minor aggregation at pH 5.4, but was effectively colloidally stable at pH 3.4 and 7.4. Similarly, smooth mesoporous silica nanoparticles remained well dispersed over the pH range 3.4–7.4 (Fig. 1B). Despite the inherent uncertainty of the ζ-potentials observed for these systems, we thus note a good correlation between effective ζ-potential and DLS results.

Binding of the TiO_2 nanoparticles to the mesoporous silica nanoparticles reduces the effective negative charge of the latter, most clearly seen at pH 3.4 and 5.4, where positively charged TiO_2 nanoparticles into/onto negatively charged silica nanoparticles resulted in charge inversion (Fig. 2). For the smooth mesoporous silica nanoparticles, the effective ζ-potential of 100 ppm of silica particles reached saturation at 25 ppm of TiO_2, whereas for the virus-like nanoparticles some further loading of TiO_2 nanoparticles occurred on increasing

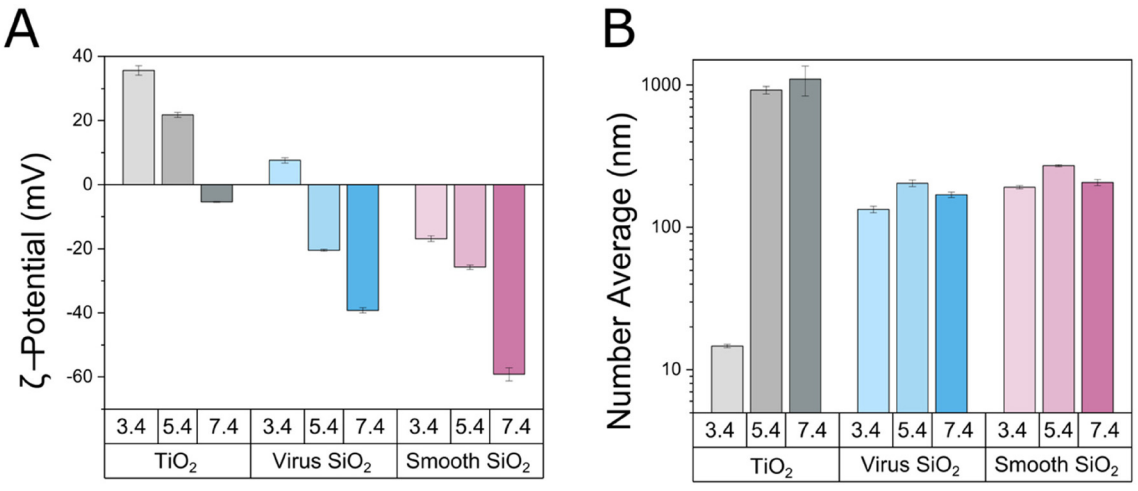

Fig. 1 Effective ζ-potential (A) and average particle size (B) of TiO_2 nanoparticles, as well as of non-loaded virus-like and smooth mesoporous nanoparticles as a function of pH, measured at a particle concentration of 100 ppm in 10 mM Acetate pH 3.4 or pH 5.4, or Tris pH 7.4. All measurements were performed in triplicate.

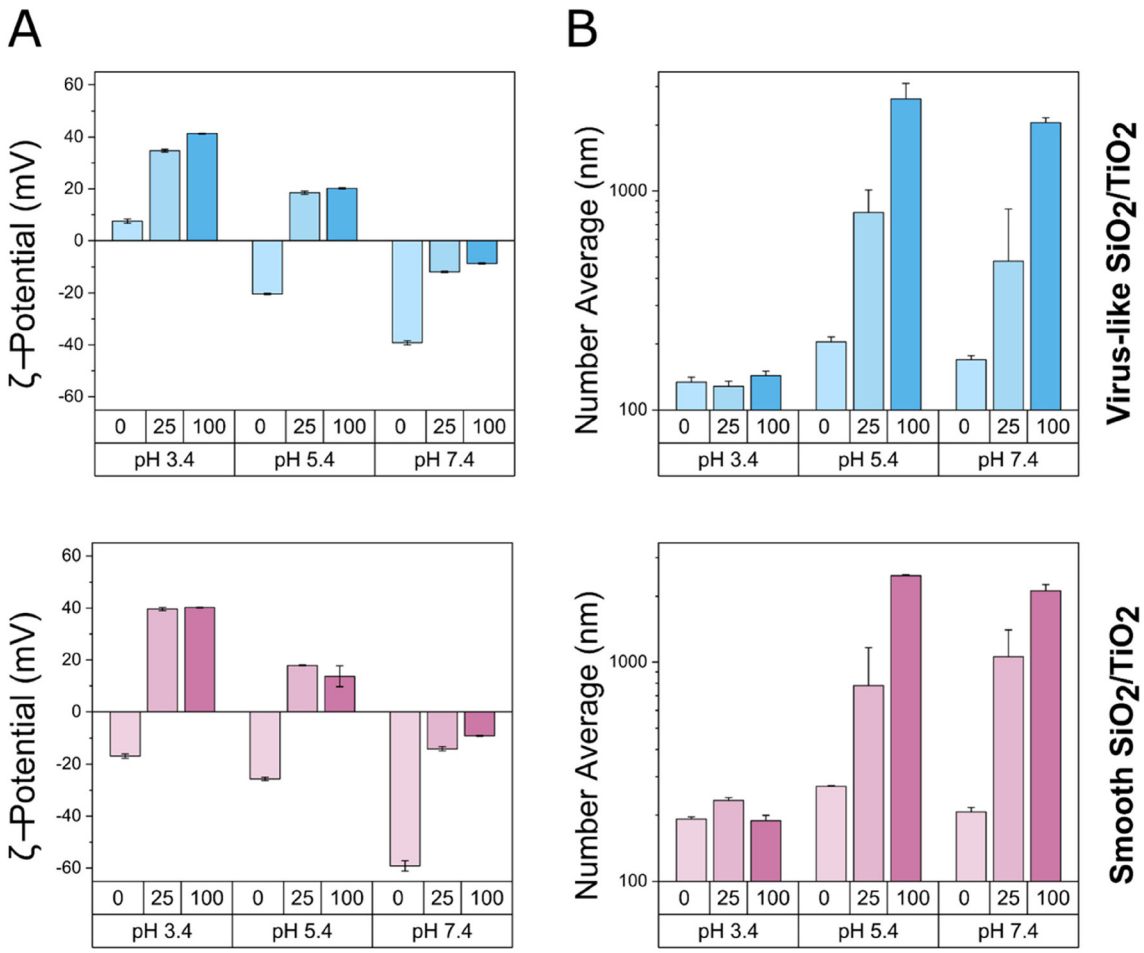

Fig. 2 Effective ζ-potential (A) and average particle size (B) of SiO_2/TiO_2 combinations for either virus-like (top) or smooth (bottom) SiO_2 nanoparticles for 0, 25, and 100 ppm TiO_2, prepared directly in 10 mM Acetate pH 3.4 or pH 5.4, or Tris pH 7.4 (*i.e.*, where the TiO_2 nanoparticles are aggregated at pH 5.4 and 7.4 before being mixed with the silica nanoparticles). All measurements were performed at 100 ppm SiO_2 nanoparticles in triplicate.

the TiO_2 nanoparticle concentration to 100 ppm. At pH 7.4, TiO_2 nanoparticles were almost neutral, hence binding of these to the mesoporous silica nanoparticles reduced the effective negative ζ-potential of the latter, but was unable to induce charge reversal (Fig. 2A). Again, a correlation was observed between DLS and effective ζ-potential results, despite the inherent uncertainties of the latter related to the complexity of the systems investigated. Importantly, however, colloidal stability was directly observed by DLS, and not affected by any assumptions of absolute ζ-potentials. Thus, mirroring the aggregation of TiO_2 nanoparticles alone at pH 5.4 and 7.4, mixtures of TiO_2 nanoparticles and the mesoporous silica nanoparticles (formed directly at pH 5.4 or 7.4, *i.e.*, with TiO_2 in pre-aggregated form) displayed colloidal instability, which was accentuated by increasing concentration of TiO_2 nanoparticles. In contrast, for TiO_2 nanoparticles loaded into either virus-like or smooth mesoporous silica nanoparticles at pH 3.4 (*i.e.*, with TiO_2 nanoparticles well-dispersed), the loaded composite particles remained well-dispersed at pH 3.4 up to a TiO_2 loading of at least 25 ppm for 100 ppm dispersions of the silica nanoparticles (Fig. 3). DLS thus demonstrates that the majority of TiO_2 nanoparticles are bound to both the smooth and the virus-like mesoporous silica nanoparticles at pH 3.4 and 5.4, since particle size the massive aggregation displayed by free TiO_2 at this pH (aggregates of the order of 1000 nm or more) is largely suppressed after loading of 25 ppm TiO_2 to 100 ppm silica nanoparticles. Having said that, there is indeed a smaller fraction of free TiO_2 nanoparticles at pH 5.4 in particular, and less so at pH 3.4, able to undergo aggregation (Fig. S2 and S3†). Once these are removed, the remaining composite systems remain colloidally stable at pH 5.4 as well. This means that the loading of TiO_2 nanoparticles in the mesoporous silica nanoparticles is slightly lower than 20 wt/wt % at pH 3.4 and 5.4, but considerably lower than that at pH 7.4 due to electrostatically triggered expulsion of TiO_2 nanoparticles at this pH.

Providing further information on the mixed TiO_2 silica nanoparticle systems, cryo-TEM results show TiO_2 nanoparticles alone were prone to aggregation, with some clusters formed already at pH 3.4, but massive aggregation occurring at

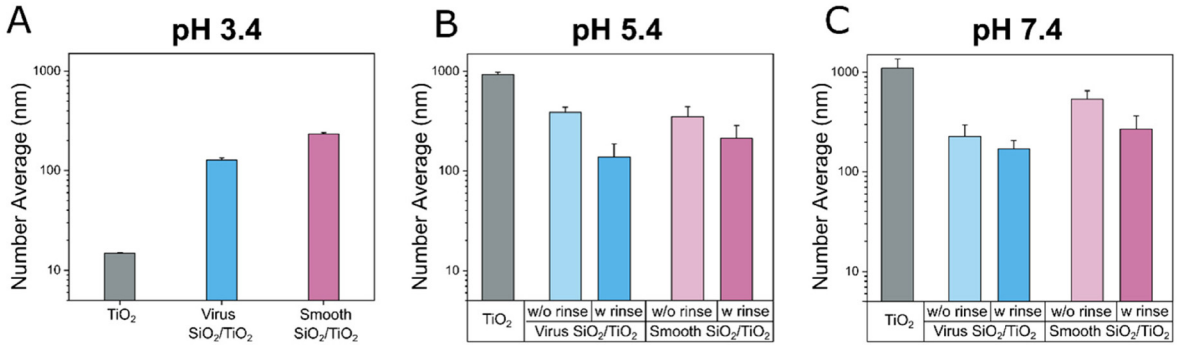

Fig. 3 Average particle size of free TiO_2 and 100/25 ppm SiO_2/TiO_2 combinations with either virus-like or smooth SiO_2 nanoparticles. Samples were prepared at pH 3.4 (*i.e.*, where the TiO_2 nanoparticles were well-dispersed), after which pH was increased to 5.4 or to 7.4. The effective average size of samples was measured before (w/o) and after (w) rinse at pH 5.4 and 7.4. All measurements were performed at 100 ppm SiO_2 nanoparticles in triplicate.

pH 7.4 (Fig. S4†). In contrast, both virus-like and smooth mesoporous silica nanoparticles at 100 ppm in pH 3.4 were able to internalize TiO_2 nanoparticles up to a concentration of 25 ppm, with no free TiO_2 particles shown in the micrographs for the virus-like nanoparticles and only very few for the smooth ones. At a TiO_2 addition of 100 ppm, on the other hand, neither of the silica nanoparticles were able to fully capture all TiO_2 nanoparticles, and the excess of the latter can be seen surrounding the silica particles (Fig. 4). This is in line with a loading capacity of about 20 wt/wt % or slightly lower. At pH 7.4, the reduced charge of the TiO_2 nanoparticles triggered release of TiO_2 nanoparticles from both types of silica nanoparticles. As shown in Fig. S2 and S3,† the release of TiO_2 nanoparticles and subsequent aggregation of the latter on increasing pH, can be seen also by DLS. Interestingly, however, rinsing allowed released TiO_2 nanoparticles to be removed and silica nanoparticles with remaining TiO_2 nanoparticles to remain well-dispersed. Taken together, these results thus show that TiO_2 nanoparticles can be incorporated into/onto both virus-like and smooth mesoporous silica nanoparticles at pH 3.4, thereby reaching improved colloidal stability at close-to-neutral pH. Furthermore, the quantitative uptake at pH 3.4 of 25 ppm TiO_2 nanoparticles in both types of silica nanoparticles at 100 ppm means that the TiO_2 loading of smooth

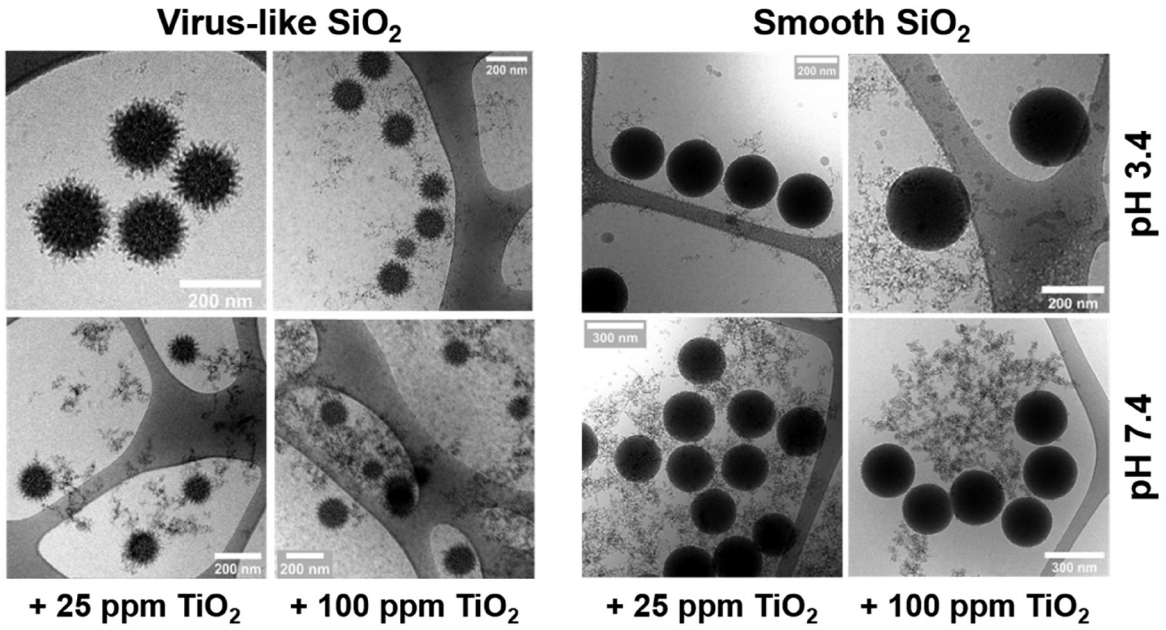

Fig. 4 Cryo-TEM images of virus-like (left) and smooth (right) mesoporous SiO_2 nanoparticles (100 ppm) combined with either 25 or 100 ppm of TiO_2 nanoparticles at pH 3.4 and pH 7.4. At pH 3.4, TiO_2 nanoparticles are bound to/incorporated into both smooth and virus-like silica nanoparticles up to a concentration of 25 ppm TiO_2 in 100 ppm silica nanoparticles. At higher concentrations of TiO_2, free TiO_2 nanoparticles appear, indicating that saturation binding between 25 and 100 ppm TiO_2. At pH 7.4, decreased charge contrast between TiO_2 and silica nanoparticles results in release of some of the TiO_2 nanoparticles, effects again seen for both smooth and virus-like silica nanoparticles.

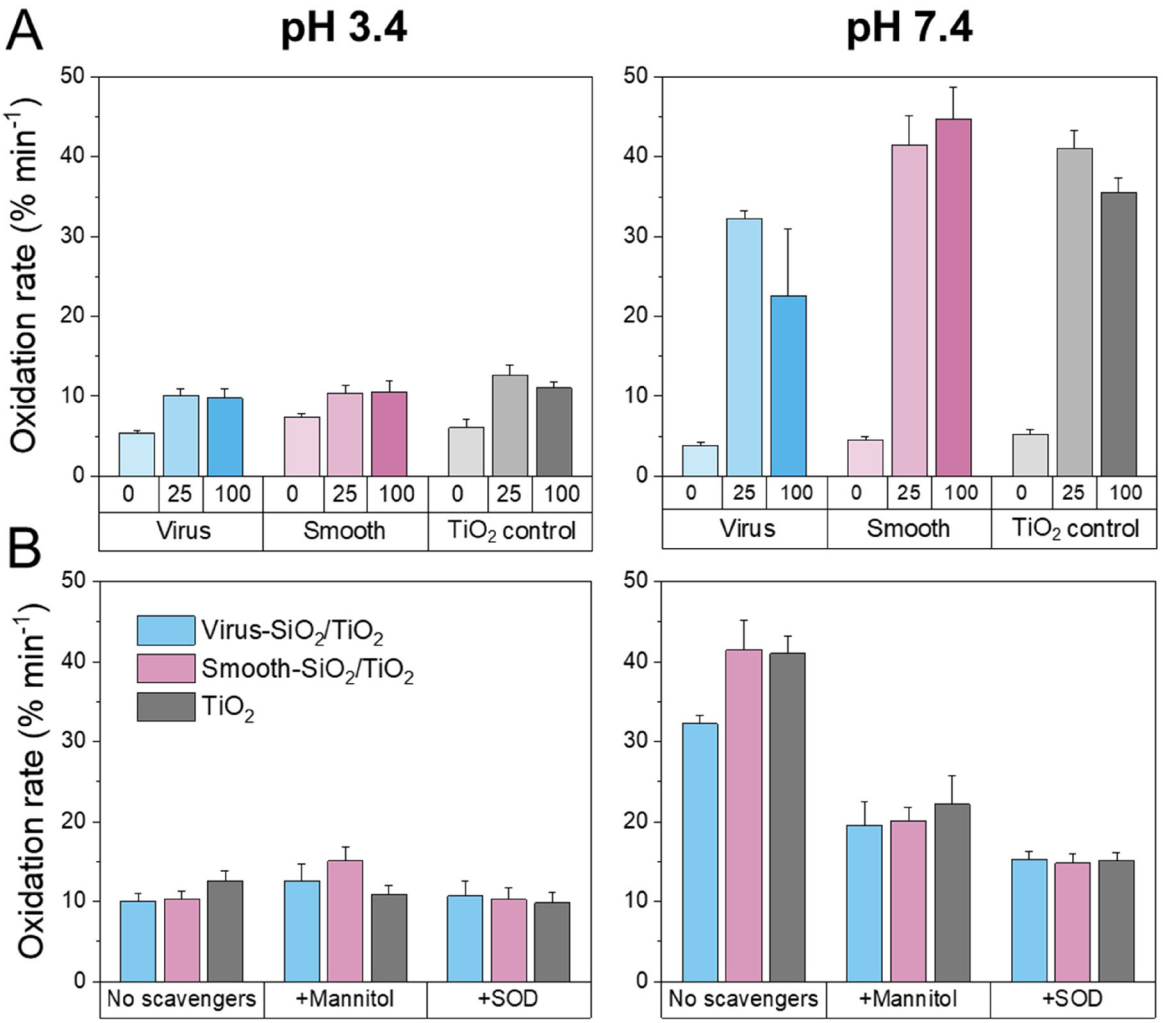

Fig. 5 (A) Oxidation rates calculated from C_{11}-BODIPY oxidation assay, showing the effect of SiO_2/TiO_2 combinations consisting of 100 ppm of either virus-like or smooth SiO_2 nanoparticles with increasing TiO_2 concentration (0, 25, 100 ppm), as well as of free TiO_2 nanoparticles (25 ppm), on POPC/PAPC/POPG (50/25/25) unilamellar liposomes subjected to *in situ* UV exposure in 10 mM buffer pH 3.4 (left) and pH 7.4 (right). (B) Effect of addition of the free radical scavengers D-mannitol ($^{\bullet}OH$ scavenger, 100 mM) and SOD (superoxide inhibitor, +10 U mL^{-1}) on oxidation rates for the different 100/25 SiO_2/TiO_2 nanoparticle combinations at pH 3.4 (left) and pH 7.4 (right). Measurements were performed in triplicate.

and virus-like silica nanoparticles are similar in the neutron reflectometry experiments described below.

ROS generation and lipid oxidation

Next, lipid oxidation triggered by UV illumination was investigated. As shown in Fig. 5A and Fig. S5,† oxidation in the absence of TiO_2 nanoparticles was very low, about 5 ± 2%, for both the smooth and the virus-like mesoporous silica nanoparticles. This is very similar also to background oxidation in aqueous solution, *i.e.*, in the absence of both TiO_2 and silica nanoparticles. On loading the silica nanoparticles (100 ppm) with TiO_2 nanoparticles (25 ppm), increased oxidation was expectedly observed, an effect which, however, was not further accentuated on increasing the TiO_2 load to 100 ppm. As observed previously,[16] the oxidation rate monitored by C_{11}-BODIPY was substantially higher at pH 7.4 than at pH 3.4, an effect possibly influenced by hydroxyl radicals converting into their less reactive conjugate base at low pH, although protonation of the superoxide radical below pH 4.8 may balance such effects.[30] At pH 7.4, the oxidation rate was found to be slightly lower for TiO_2 loaded into virus-like nanoparticles than that for either free TiO_2 or TiO_2 loaded into smooth mesoporous silica nanoparticles, although at pH 3.4, no differences between these were observed. In order to obtain information of ROS species generated on UV illumination of these systems, experiments were performed also in the presence of ROS scavengers, *i.e.*, D-mannitol ($^{\bullet}OH$ scavenger)[19] and SOD (superoxide inhibitor).[20] As shown in Fig. 5B and Fig. S6,† both D-mannitol and SOD results in suppressed oxidation rate at pH 7.4, showing both $^{\bullet}OH$ and $O_2^{\bullet-}$ to be formed during UV illumination of these systems and participating in C_{11}-BODIPY oxidation. Again, TiO_2 nanoparticles loaded into either virus-

like or smooth mesoporous silica nanoparticles displayed similar oxidation rates to those displayed by free TiO_2 nanoparticles.

Consequences of lipid oxidation for membrane structure and destabilization

In order to obtain information on how lipid oxidation translates into structural changes in the lipid bilayers, NR experiments were next performed for supported PC/PG bilayers in the absence and presence of either free TiO_2 nanoparticles or TiO_2 nanoparticles loaded into smooth or virus-like mesoporous silica nanoparticles, both in the absence and presence of UV illumination. Experiments were performed in 10 mM acetate buffer, prepared both in H_2O (hAcet) and D_2O (dAcet), at pH 3.4, as this was the pH at which the most pronounced effects were observed, and where effects of free TiO_2 nanoparticles were minimized. The two contrasts used to measure the bilayers were fitted simultaneously to a 4-layer model using the method previously described and the input parameters shown in Table S1† (Model 1 in Scheme S1†). Due to the difficulty of unambiguously decoupling differences in thickness from differences in the roughness of the hydrogenated material, and to reduce the number of free parameters, head group thicknesses were fixed at 7.5 Å.[31] An extra constraint was also used in the model, where the heads and the tails must occupy the same area. In all cases, the initial bilayers presented >99% coverages and low (~0%) tail hydration. The fit results for the PC/PG bilayers before exposure to any nanoparticles are shown in Table S2.† The thickness (45 ± 1 Å), area per molecule (APM = 61 ± 2 $Å^2$) and surface coverage (Γ = 4.1 ± 0.1 mg m^{-2}) values were calculated as previously described,[16] and are consistent with previous literature values.[32,33]

Shown in Fig. 6 are reflectivity data as well as SLD values extracted from these, while full structural data calculated from the fits are listed in Tables S2 and S3.† In the absence of UV illumination, only minor changes were observed for both free TiO_2 nanoparticles and TiO_2 nanoparticles loaded into either smooth or virus-like silica nanoparticles (Fig. 7A). Thus, the APM for the PC/PG bilayer changed from 61 ± 2 $Å^2$ before nanoparticle addition to 66 ± 2, 66 ± 3, and 69 ± 2 $Å^2$ for after addition of TiO_2, TiO_2 loaded into smooth silica nanoparticles, and TiO_2 loaded into virus-like silica nanoparticles, respectively. Contrasting these minor effects, pronounced charges were observed for all three TiO_2-containing systems under UV exposure. While UV illumination for 2 h and final buffer rinsing only slightly reduced the final bilayer thickness (from 45 ± 1 Å to 43 ± 1, 45 ± 1, and 42 ± 1 Å for free TiO_2, TiO_2 loaded into smooth silica nanoparticles, and TiO_2 loaded into virus-like silica nanoparticles respectively), hydration of both acyl chains and head groups increased significantly. As a consequence of this, the final APM values increased strongly, from

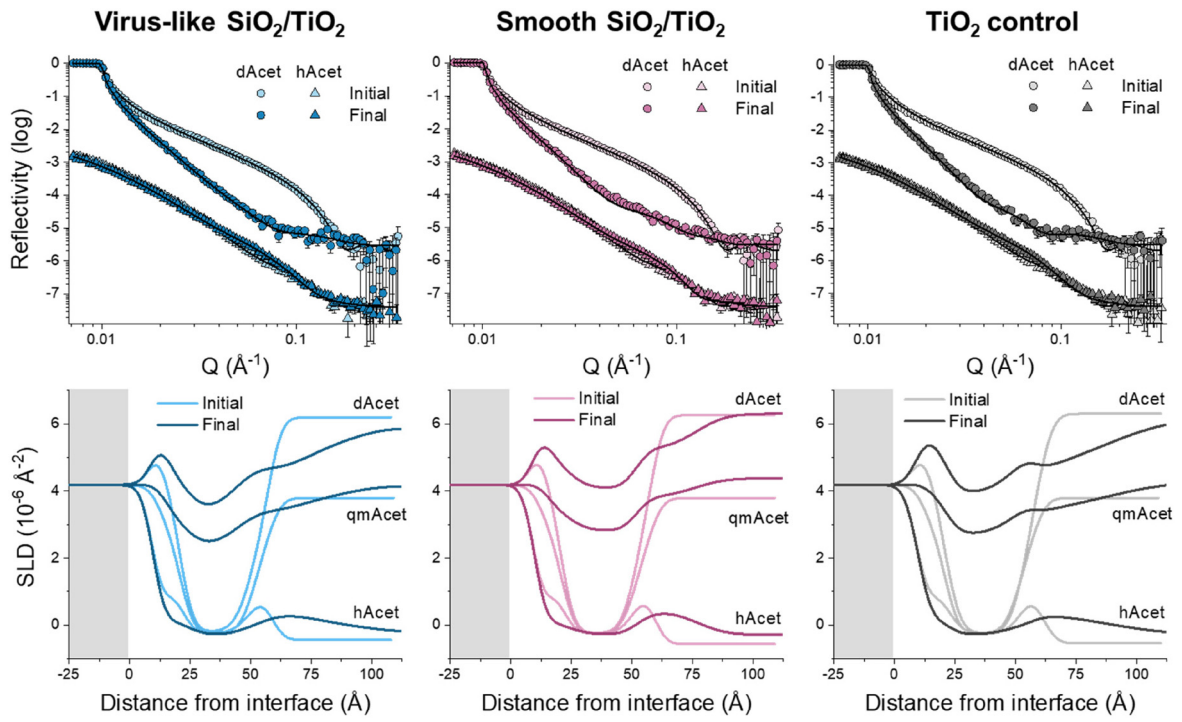

Fig. 6 Neutron reflectivity curves with best model fits (upper) and SLD profiles (lower) obtained for supported POPC/PAPC/POPG bilayers before and after incubation with TiO_2-loaded virus-like (left) and smooth mesoporous SiO_2 nanoparticles (middle), as well as with free TiO_2 nanoparticles (right), 2 h of *in situ* UV exposure, and final rinsing, all performed in 10 mM acetate buffer pH 3.4. Curves are shown for two different buffer contrasts, dAcet and hAcet, and the data for the latter are offset by 10^{-2} for clarity. The grey box in the SLD profiles indicates the position of the silicon block and reflecting interface, consisting of bulk Si and a SiO_2 layer, and all three buffer contrasts used, dAcet, hAcet and qmAcet, are shown.

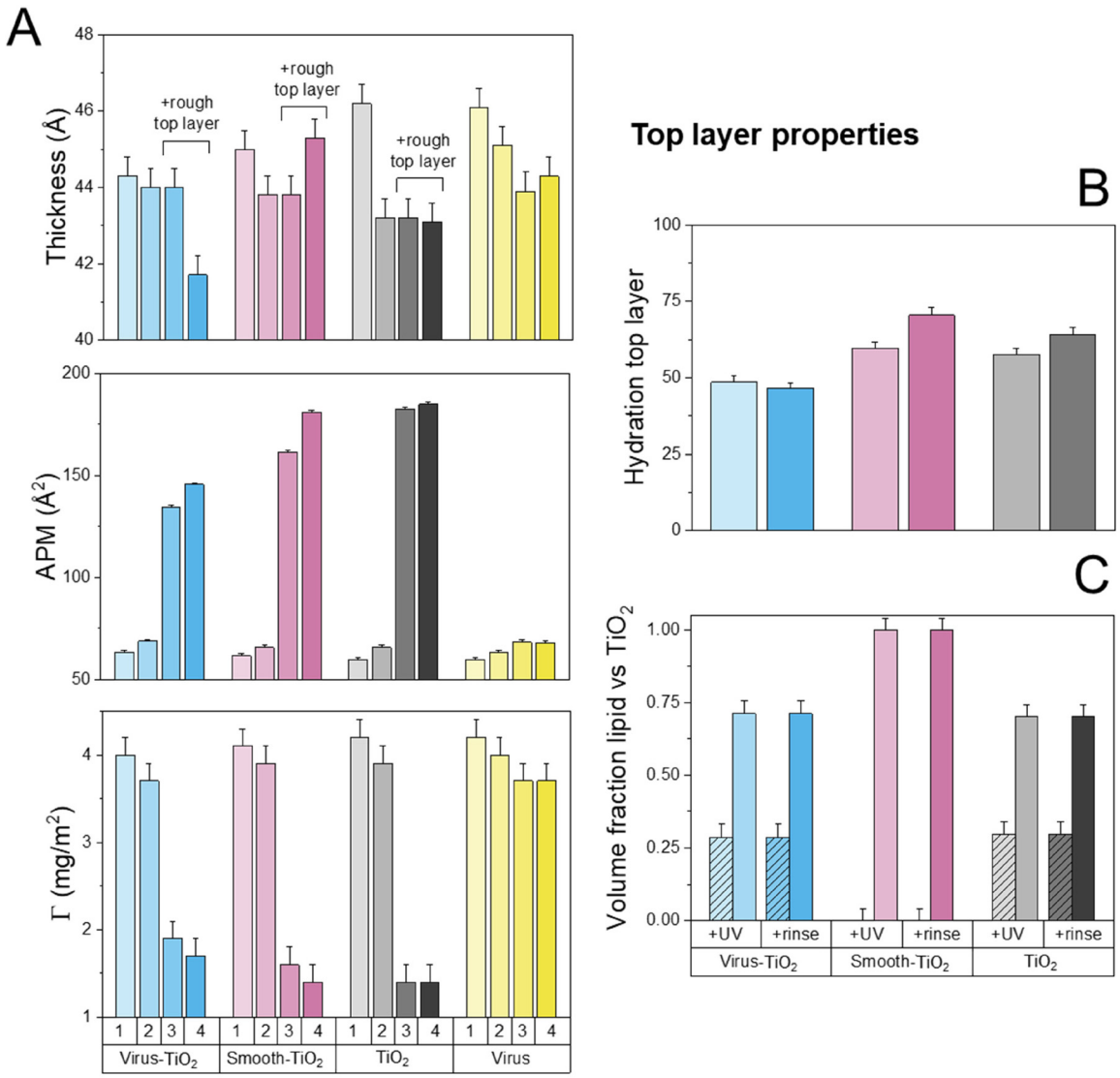

Fig. 7 (A) Structural and compositional effects on supported POPC/PAPC/POPG bilayers of 100/25 ppm virus-like or smooth SiO_2/TiO_2 combinations, as well as of free TiO_2 nanoparticles (25 ppm), obtained from neutron reflectometry fits, calculating the physical parameters of the bilayers at different time points: (1) before incubation with the nanoparticles; (2) after incubation with the nanoparticles; (3) immediately after 2 h of *in situ* UV exposure; (4) and after final rinsing. Experiments were performed in 10 mM Acetate buffer, pH 3.4. Shown in A are changes in thickness (top), area per molecules (APM, middle), and surface coverage of the supported lipid bilayer (Γ, bottom). Shown also are result on top layer hydration (B), as well as volume fractions of lipid (patterned bars) and TiO_2 nanoparticles (clear bars) (C) of the top layer obtained from the fittings and SLD values.

61 ± 2 Å^2 to 185 ± 6, 181 ± 5 and 146 ± 3 Å^2 for free TiO_2, TiO_2 loaded into smooth silica nanoparticles, and TiO_2 loaded into virus-like silica nanoparticles, respectively. These values correspond to final surface coverages of 1.4 ± 0.2, 1.4 ± 0.2 and 1.7 ± 0.2 mg m^{-2}, respectively, therefore pointing to extensive lipid removal triggered by both free and silica-bound TiO_2 nanoparticles. In the latter cases, the bilayers contained truncated and/or oxidized lipid metabolites that were water-soluble and could be removed by rinsing with buffer. As shown previously, smooth mesoporous silica nanoparticles do not cause any binding or destabilization of anionic PG-containing bilayers.[15] Furthermore, as shown in Fig. S7,† virus-like mesoporous silica nanoparticles do not display any UV-triggered destabilization of such bilayers. Thus, the photocatalytic effects in for TiO_2/silica composite particles can be ascribed solely to the TiO_2 nanoparticles.

As seen above, the bilayer thickness remained largely unaffected under oxidative degradation, while hydration and APM both increased strongly. These results therefore report on lipid removal from the supported bilayer, although the process is slightly more complex than this. Thus, a rough outer layer was necessary to include to fit the experimental data (Model 2 in Scheme S1†), as previously described by us for free TiO_2 nanoparticles.[16] As shown in Fig. 7B, the hydration of this top layer was comparable, although slightly higher, for TiO_2 nanoparticles loaded into either smooth or virus-like silica nano-

particles than for free TiO_2 nanoparticles. Composition-wise, the volume fraction of lipid to TiO_2 was comparable for free TiO_2 and TiO_2 loaded into the virus-like nanoparticles, and slightly higher for TiO_2 loaded into the smooth nanoparticles (Fig. 7C), although the likely simultaneous presence of silica and TiO_2 nanoparticles (of different SLD; Table S1†) in this layer precludes closer analysis.

In the absence of TiO_2 nanoparticle loading, the virus-like silica nanoparticles only caused limited increases in hydration and APM values (68 ± 2 Å^2) on UV exposure (Fig. S7 and S8†), comparable to those previously observed by us for UV exposure alone.[16,17] Therefore, the effect of the silica surface topography in the absence of TiO_2 did not show a significant effect on top of the UV effect.

In order to investigate the kinetics of these effects, reflectivity changes during UV exposure were monitored over a narrower Q-range, allowing faster data acqusition.[34] Still, the Q-range included the area around critical edge at Q ~ 0.01 Å^{-1} to continuously monitor its position and be able rule out major SLD changes in the bulk solution, for instance due to air bubble formation. As shown in Fig. 8, pronounced decreases in reflectivity over time were observed for both free TiO_2 nanoparticles and TiO_2 nanoparticles loaded into either smooth or virus-like silica nanoparticles. Analysis of these results showed that the bilayer thickness remained essentially constant for all three systems investigated during exposure for 120 min, in agreement with the results discussed above. With regards to changes in APM during UV exposure, a multi-stage process was observed, where increases for the first 20 min were essentially identical for the three systems. After that, oxidative lipid removal was accelerated during the subsequent 20–30 min of UV exposure, followed by a gradual leveling off, as seen most clearly for TiO_2 loaded into the virus-like nanoparticles.

Discussion

As many other nanomaterials, TiO_2 nanoparticles may destabilize bacterial membranes through direct binding and membrane destabilization.[2,3] What makes these nanoparticles particularly interesting as antimicrobial agents, however, is their ability to oxidize lipids and other membrane components under UV illumination.[4,5] While UV-induced antimicrobial effects have been frequently reported in literature, and while these have been correlated to oxidative degradation of membrane lipids[35–37] and other bacterial membrane components such as peptidoglycan and lipopolysaccharide (LPS),[38] the mechanisms by which membrane component oxidation translates into membrane destabilization remain largely unresolved. Considering this, we previously investigated effects of ambient conditions and membrane composition on photocatalytic destabilization of phospholipid membranes by TiO_2 nanoparticles, employing a battery of physicochemical techniques. While cholesterol was found to provide stabilization against TiO_2-triggered oxidation of PC-based bilayers, the presence of anionic PG made these bilayers more sensitive to oxidative destabilization, likely an effect of less dense packing, and/or the occurrence of different free-radical processes.[17] Neutron reflectometry and small-angle X-ray scattering furthermore showed that lipid oxidation caused by UV illumination of TiO_2 nanoparticles triggered pronounced structural changes of the bilayers, including increased hydration, lipid removal, bilayer thinning, lateral phase separation, and aggregate solubilization.[16,17] In comparison, UV exposure in presence of H_2O_2 but in the absence of TiO_2 nanoparticles resulted in quantitatively smaller effects.[39] Extending on these previous studies on free TiO_2 nanoparticles, the present study shows that qualitatively similar effects are obtained for TiO_2 nanoparticles incorporated into larger matrix particles, such as mesoporous silica nanoparticles.

As discussed above, DLS results showed colloidal stability when loading TiO_2 nanoparticles into SiO_2 nanoparticles at pH 3.4 (*i.e.*, when the TiO_2 nanoparticles are well-dispersed) and subsequently increasing pH to 5.4 after loading, but not when loading the TiO_2 nanoparticles directly at pH 5.4 (*i.e.*, when the TiO_2 nanoparticles are pre-aggregated), thus demonstrating TiO_2 nanoparticle incorporation to the SiO_2 nanoparticles at pH 3.4. Quantitatively, both DLS and cryo-TEM results show TiO_2 nanoparticle incorporation to both smooth and virus-like nanoparticles up to a maximal loading of slightly less than 20 wt/wt %, and that the majority of these remain bound also when increasing pH to 5.4 after loading at pH 3.4. For overall colloidal stability to be reached, however, also the TiO_2-loaded mesoporous silica nanoparticles must be well-dispersed. At pH 5.4, the effective ζ-potential of the TiO_2 and the silica particles are +20 ± 2 and −27 ± 3 mV, respectively, whereas those of the silica nanoparticles loaded with TiO_2 nanoparticles at 25 ppm/100 ppm are about 20 mV for both the smooth and the virus-like nanoparticles at the same pH. From a general perspective, the electrostatic potential required to reach colloidal stability depend also van der Waals interactions, which in turn depend on particle size, shape, and dielectric constant. In particular, the mesoporous silica nanoparticles contain a considerable pore volume (as evidenced by the capacity of these to load smaller peptides up to a loading of 0.9 g g^{-1}[5], which are mostly filled with water (TiO_2 nanoparticle loading slightly less than 20 wt/wt %)). As a result of this, attractive van der Waals interactions are significantly suppressed compared to that of solid Stöber particles, hence a smaller magnitude electrostatic repulsion is needed to ensure colloidal stability. Again, however, the inherent uncertainty of the ζ-potential values for the mesoporous SiO_2 and TiO_2/SiO_2 systems should be remembered here. Hence, colloidal stability needs to be monitored directly from particle size measurements, as done by DLS in the present study.

In the absence of surface spikes, mesoporous silica nanoparticles do not destabilize PG/PC bilayers.[15] For TiO_2-loaded smooth silica nanoparticles, membrane destabilization is therefore expected to be caused only by oxidative action of ROS induced by UV illumination. For TiO_2 nanoparticles incorporated into such particles, photocatalytic effects could, however,

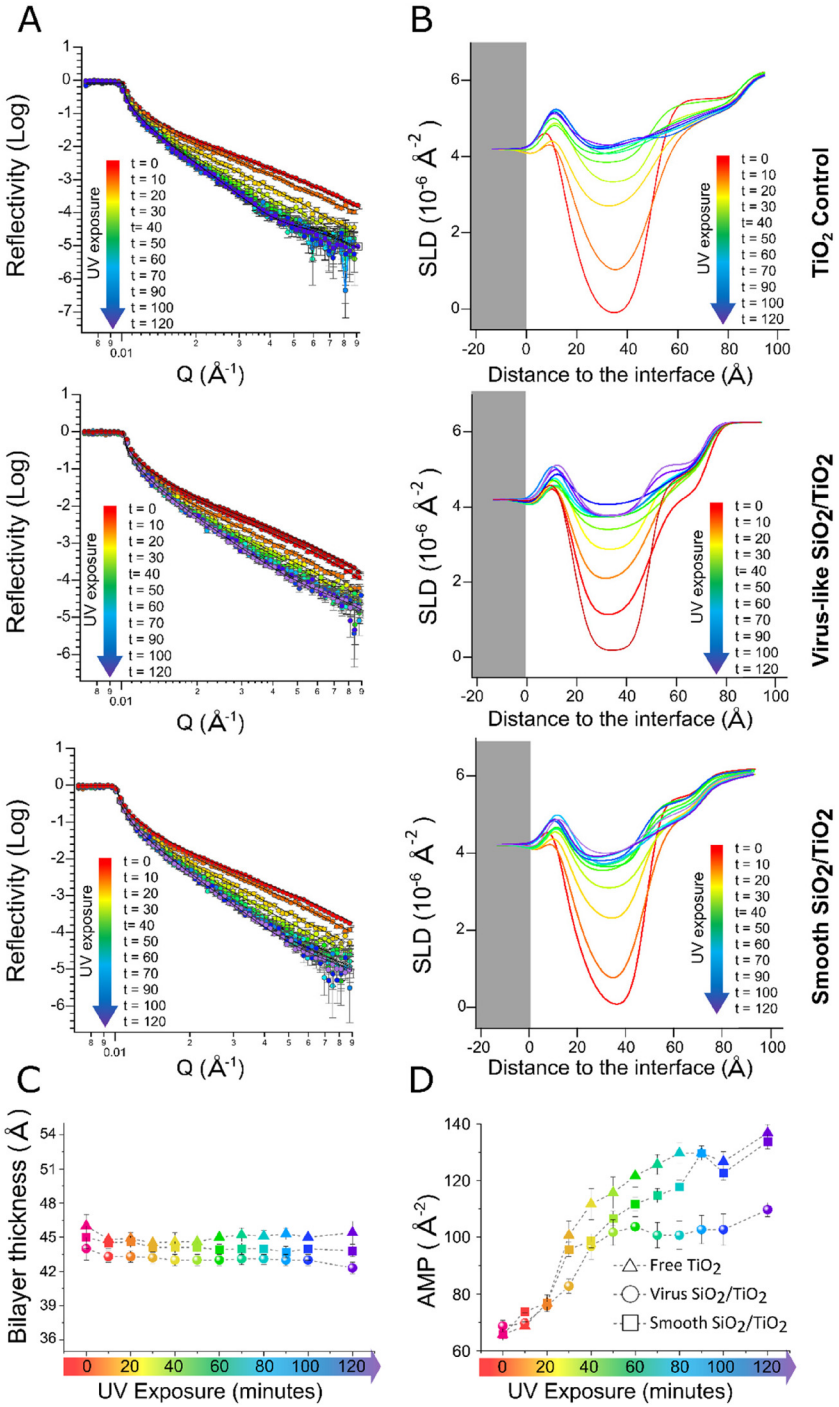

Fig. 8 Neutron reflectivity curves and best fits (A) for TiO_2 NPs (25 ppm), either free or bound to (100 ppm) of virus-like or smooth silica nanoparticles, as well as corresponding SLD (B). Shown also are the calculated bilayer thickness (C) and area per molecule, *i.e.*, AMP, (D) at different time points before, during and after 2 h of UV exposure.

potentially be affected by several factors. First, the matrix particles absorb some of the UV light, which in turn may result in reduced ROS formation.[40] Furthermore, depending on TiO_2 localization within the silica nanoparticles, the diffusion length of ROS generated at the TiO_2 surface before reaching the membrane lipids will be longer, which risks resulting in a reduced fraction of ROS reaching the membrane surface.[30] As proximity between TiO_2 nanoparticles and the membrane has previously been found to be important for UV-induced membrane destabilization,[16,17] ROS diffusion length/life time effects could potentially result in suppressed photocatalytic destabilization of lipid membranes for TiO_2 loaded into the

silica particles. Such effects are expected to be larger for virus-like mesoporous silica nanoparticles due to their outer shell of spikes. On the other hand, incorporation of TiO_2 nanoparticles into mesoporous silica nanoparticles suppress colloidal destabilization of the former, which may result in an effectively increased TiO_2-water surface area, thus favoring ROS generation.[41] However, the binding of TiO_2 nanoparticles to the mesoporous silica matrix may also affect re-combination between photogenerated electrons and holes,[42] which would also influence ROS generation and UV-induced lipid oxidation and membrane destabilization.

In contrast to smooth mesoporous nanoparticles, which do not substantially destabilize anionic membranes in the absence of UV, virus-like nanoparticles can induce direct membrane destabilization induced by the spikes on the latter, previously investigated by Malekkhaiat Häffner *et al.*[15] This direct membrane destabilization may potentially compensate for losses in photocatalytic membrane destabilization on incorporating TiO_2 nanoparticles into mesoporous silica nanoparticles. Analogously, Lu *et al.* investigated membrane interaction of graphene oxide nanosheets as a function of the orientation the latter. Exposing *Escherichia coli* (*E. coli)* bacteria to surfaces coated with graphene oxide nanosheets in a vertical orientation (*i.e.*, with the sharp edge oriented towards the solution) was found to result in higher antibacterial activity than nanosheets in either random orientation or lying flat at the surface, illustrating the importance of direct nanosheet-mediated membrane destabilization. In addition, ROS generation and oxidative membrane destabilization were observed, illustrating an interplay between these effects.[43] Analogously, Huang *et al.* showed the antimicrobial effects of fullerenes against *E. coli* and *Staphylococcus aureus* to correlate with the partitioning of fullerenes into bacterial membranes. However, such antimicrobial effects caused by direct particle-mediated membrane destabilization could be substantially enhanced by photocatalytic effects,[44] as also reported by Lyon *et al.*[45] Similarly demonstrating the interplay between particle-mediated and oxidative membrane destabilization, Vecitis *et al.* investigated single-walled carbon nanotubes (SWCNTs) with different levels of defects, and found both glutathione oxidation and morphological changes to depend on the electronic structure of the SWCNTs, notably increasing with their metallic nature and oxidative capacity.[46] Also, along the same line, Cui *et al.* investigated the effect of nitrogen plasma treatment of graphitic carbon nitride nanosheets, g-C_3N_4 (N-g-C_3N_4) on their antimicrobial effects against foodborne bacteria, and found bactericidal activities in the dark >10 times higher than those for g-C_3N_4, an effect related to boosted membrane binding after cationization. However, bacterial rupture was also correlated to the abundance of surface defects and nitrogen vacancies in N-g-C_3N_4, and hence also to photocatalytic effects.[47] In contrast to these previous findings, the results of the present investigation show that direct membrane destabilization by the spikes of the virus-like nanoparticles only marginally influences the photocatalytic effects of TiO_2. There are several reasons for this. In comparison to carbon-based nanomaterials such as g-C_3N_4, CNTs, and fullerenes, and graphene derivatives, mesoporous silica nanoparticles are characterized by very low optical absorption, hence loss of light needed to generate free electrons and holes in TiO_2 after incorporation into silica matrices is expected to be minor. Hence, photocatalytic effects of the silica-loaded TiO_2 nanoparticles are correspondingly larger and direct membrane interactions relatively less important. In fact, TiO_2 nanoparticles loaded into the virus-like silica nanoparticles trigger slightly *lower* photocatalytic effects than either free TiO_2 or TiO_2 loaded into mesoporous silica nanoparticles. Here, one need to be careful to exclude effects of colloidal instability, as aggregation would result in reduced surface area, which in turn may result in an increased probability of charge recombination (and hence suppressed ROS generation),[48] as well as diffusion limitations of ROS formed. Having said that, the results (DLS as well as cryo-TEM at pH 3.4) do not support the notion of colloidal instability causing the slower kinetic observed for the virus-like nanoparticles (but not the smooth ones) compared to that of free TiO_2, as all these systems are well-dispersed at the conditions employed for the neutron reflectometry experiments. Instead, the slightly slower kinetics observed for the virus-like nanoparticles is likely an effect of the spikes, which effectively increase the diffusion length of ROS generated within the TiO_2-loaded silica matrix to reach the target membrane lipids, in line with the slightly lower ROS generation observed for TiO_2 nanoparticles loaded into the virus-like particles (Fig. 5A), which in turn contributes to the slightly slower oxidative membrane destabilization (Fig. 8D).

While the relative importance of these effects for different photocatalytic nanoparticles and matrices needs to be further investigated, the findings of the present study show that TiO_2 nanoparticles can indeed be incorporated into mesoporous silica nanoparticles for improved colloidal stability at largely retained photocatalytic effects with largely retained photocatalytic activity, as well as similar modes-of-action for destabilizing bacteria-mimicking lipid membranes (Fig. 9).

Finally, we note that the broader applicability of the approach taken will need to be investigated in biological effect studies. In order to provide meaningful and conclusive results, antibacterial effects need to be studied in a comprehensive study design. Rather than just selecting an arbitrary example and experimental setup, such effects need to be investigated for several bacterial strains, and also under various bacteria densities and ambient conditions. Since the relative effects of UV exposure alone, nanoparticles alone, and nanoparticles under UV exposure vary with particle concentration, illumination time, and illumination distance, these parameters need to be investigated as well. Furthermore, since photocatalytic nanoparticles may cause oxidative degradation not only of bacteria, but also eukaryotic cells, antimicrobial effects need to be compared to effects on cell toxicity, again requiring several cell types and assays in order to be able to generate results of broader validity. We are currently working on such an extensive biological effect study for TiO_2 nanoparticles, to be communicated separately.

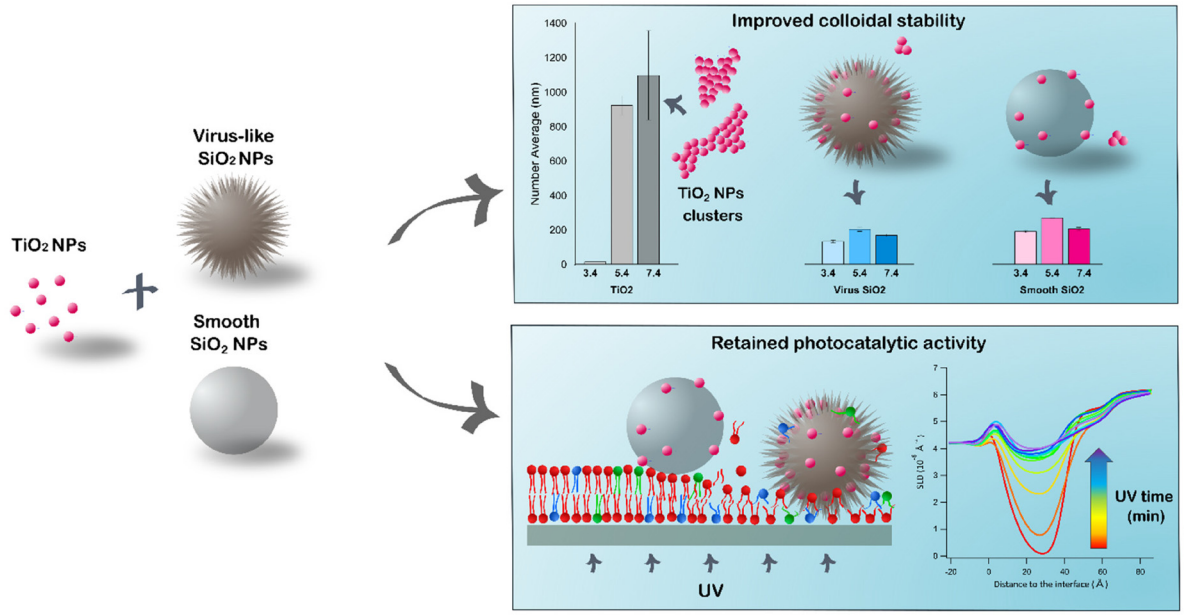

Fig. 9 Schematic illustration of the main effects associated to the loading of photocatalytic TiO_2 nanoparticles into smooth or virus-like mesoporous nanoparticles. As shown, loading of TiO_2 nanoparticles into either smooth or virus-like mesoporous silica nanoparticles suppressed their aggregation at neutral and close-to-neutral pH (upper panel) at largely retained photocatalytic efficiency (lower panel). Neutron reflectivity analyses showed that only minor destabilization occurs for all these systems in the absence of UV illumination, whereas UV illumination triggers pronounced membrane destabilization, including membrane thinning, lipid removal, and formation of a partial disordered outer membrane leaflet. Quantitatively, loading TiO_2 into virus-like silica nanoparticles resulted in slightly suppressed lipid membrane destabilization, likely due to reduced photoexcitation of TiO_2, as well as longer diffusion length of UV-triggered reactive oxygen species.

Conclusions

Consequences of incorporation of TiO_2 nanoparticles in mesoporous silica nanoparticles for colloidal stability, as well as for their photocatalytic ability to oxidize phospholipids and destabilize their membranes, were investigated by neutron reflectometry, cryo-TEM, lipid oxidation assays, and dynamic light scattering. At low pH, charge contrast between silica and TiO_2 nanoparticles drives loading of the latter into the former, in turn extending the pH range of colloidal stability, allowing good colloidal stability at physiological pH of skin (pH 5.4).[49] Despite this, lipid oxidation remains qualitatively similar for free TiO_2 nanoparticles and those loaded into either smooth or virus-like ('spiky') mesoporous nanoparticles, driven by both hydroxyl and superoxide radicals. Furthermore, these systems display qualitatively similar interactions with supported model membranes based on phosphatidylcholine and phosphatidylglycerol. Thus, minor destabilization of these membranes by the nanoparticles occurs in the absence of illumination, whereas dramatically increased membrane destabilization is triggered by the presence of UV illumination, including membrane thinning, lipid removal, and formation of a partial disordered outer membrane leaflet. Quantitatively, loading TiO_2 into virus-like silica nanoparticles result in slightly suppressed lipid membrane destabilization, likely an effect of an effectively longer diffusion length for ROS generated by TiO_2 loaded within the silica matrix to reach the target membrane lipids, caused by the surface spikes. The effect of membrane destabilization by the spikes of the virus-like silica particles is thus smaller than effects observed previously for sharp-edge photocatalytic materials such as graphene, CNTs, and g-C_3N_4. This is likely an effect of the low optical absorption of silica, and the correspondingly small loss of light needed to generate free electrons and holes in TiO_2 after incorporation into silica matrices. Hence, photocatalytic effects of the silica-loaded TiO_2 nanoparticles are correspondingly larger and direct membrane interactions relatively less important. Taken together, these findings extend on previous mechanistic studies on oxidative destabilization of lipid membranes by photocatalytic nanoparticles[4,16,17] by outlining how photocatalytic nanoparticles can be incorporated into other nanomaterials for increased colloidal stability and yet retain their capacity for photocatalytic destabilization of lipid membranes. As such, the study provides new information on a widely employed practice in applications of photocatalytic nanomaterials, which had so far not been investigated mechanistically.

Author contributions

EPO and MM designed the study. All authors were involved in performing the experiments and the interpretation of the experimental results. EPO and MM wrote the paper. All authors reviewed the paper.

Conflicts of interest

There are no conflicts to declare.

Acknowledgements

We acknowledge the Core Facility for Integrated Microscopy (CFIM), Faculty of Health and Medical Sciences, University of Copenhagen, particularly Tillmann Hanns Pape, for their help and support with cryo-TEM sample preparation and imaging. We also thank ISIS (Experiment number RB2010363; **https://doi.org/10.5286/ISIS.E.RB2010363**) for access to neutron beam time and solid–liquid interface cells. The research was funded by the Swedish Research Council (Grant number 2016-05157 and 2021-05498; MM), Independent Research Fund Denmark (Grant number 9040-00020B; MM, LC, and EPO), as well as the LEO Foundation Center for Cutaneous Drug Delivery (Grant number 2016-11-01; MA and MM).

References

1 S. B. Zaman, M. A. Hussain, R. Nye, *et al.*, A review on antibiotic resistance: alarm bells are ringing, *Cureus*, 2017, **9**(e1403), 1–9.
2 S. Malekkhaiat Häffner and M. Malmsten, Membrane interactions and antimicrobial effects of inorganic nanoparticles, *Adv. Colloid Interface Sci.*, 2017, **248**, 105–128.
3 N.-Y. Lee, W.-C. Ko and P.-H. Hsueh, Nanoparticles in the treatment of infections caused by multidrug-resistant organisms, *Front. Pharmacol.*, 2019, **10**(1153), 1–10.
4 E. Parra-Ortiz and M. Malmsten, Photocatalytic nanoparticles – from membrane interactions to antimicrobial and antiviral effects, *Adv. Colloid Interface Sci.*, 2022, **299**, 102526.
5 P. Ganguly, C. Byrne, A. Breen and S. C. Pillai, Antimicrobial activity of photocatalysts: fundamentals, mechanisms, kinetics and recent advances, *Appl. Catal., B*, 2018, **225**, 51–75.
6 C. Regmi, B. Joshi, S. K. Ray, G. Gyawali and R. P. Pandey, Understanding mechanism of photocatalytic microbial decontamination in environmental wastewater., *Front. Chem.*, 2018, **6**(33), 1–6.
7 K. M. Reddy, S. V. Manorama and A. R. Reddy, Bandgap studies on anatase titanium dioxide nanoparticles, *Mater. Chem. Phys.*, 2003, **78**, 239–245.
8 J. Schubert and M. Chanana, Coating matters: Review on colloidal stability of nanoparticles with biocompatible coatings in biological media, living cells and organisms, *Curr. Med. Chem.*, 2018, **25**, 4553–4586.
9 T. L. Moore, L. Rodriguez-Lorenzo, V. Hirsch, S. Balog, D. Urban, C. Jud, B. Rothen-Rutishauser, M. Lattauda and A. Petri-Fink, Nanoparticle colloidal stability in cell culture media and impact on cellular interactions, *Chem. Soc. Rev.*, 2015, **44**, 6287–6305.
10 A. A. Dayem, M. K. Hossain, S. B. Lee, K. Kim, S. K. Saha, G.-M. Yang, H. Y. Choi and S.-G. Cho, The role of reactive oxygen species (ROS) in the biological activities of metallic nanoparticles, *Int. J. Mol. Sci.*, 2017, **18**(120), 1–21.
11 H. Dong, G. Zeng, L. Tang, C. Fan, C. Zhang, X. He and Y. He, An overview on limitations of TiO_2-based particles for photocatalytic degradation of organic pollutants and the corresponding countermeasures, *Water Res.*, 2015, **79**, 128–146.
12 M. A. M. Adnan, N. M. Julkapi, M. N. I. Amir and A. Maamor, Effect of different TiO_2 photocatalyst supports on photodecoloration of synthetic dyes: a review, *Int. J. Environ. Sci. Technol.*, 2019, **16**, 547–566.
13 M. Manzano and M. Vallet-Regí, Mesoporous silica nanoparticles for drug delivery, Adv, *Funct. Mater.*, 2020, **30**(1902634), 1–15.
14 W. Wang, P. Wang, X. Tang, A. A. Elzatahry, S. Wang, D. Al-Dahyan, M. Zhao, C. Yao, C.-T. Hung, X. Zhu, T. Zhao, X. Li, F. Zhang and D. Zhao, Facile synthesis of uniform virus-like mesoporous silica nanoparticles for enhanced cellular internalization, *ACS Cent. Sci.*, 2017, **3**, 839–846.
15 S. Malekkhaiat Häffner, E. Parra-Ortiz, K. L. Browning, E. Jørgensen, M. W. A. Skoda, C. Montis, X. Li, D. Berti, D. Zhao and M. Malmsten, Membrane interactions of virus-like mesoporous silica nanoparticles, *ACS Nano*, 2021, **15**, 6787–6800.
16 E. Parra-Ortiz, S. Malekkhaiat Häffner, T. Saerbeck, M. W. A. Skoda, K. L. Browning and M. Malmsten, Oxidation of polyunsaturated lipid membranes by photocatalytic titanium dioxide nanoparticles: role of pH and salinity, *ACS Appl. Mater. Interfaces Sci.*, 2020, **12**, 32446–32460.
17 S. Malekkhaiat Häffner, E. Parra-Ortiz, M. W. A. Skoda, T. Saerbeck, K. L. Browning and M. Malmsten, Composition effects on photooxidative membrane destabilization, *J. Colloid Interface Sci.*, 2021, **584**, 19–33.
18 B. O. Alan, M. Barisik and H. G. Ozcelik, Roughness effects of the surface charge properties of silica nanoparticles, *J. Phys. Chem. C*, 2020, **124**, 7274–7286.
19 H. J. Ahn, K. I. Kim, G. Kim, E. Moon, S. S. Yang and J.-S. Lee, Atmospheric-pressure plasma jet induces apoptosis involving mitochondria via generation of free radicals, *PLoS One*, 2011, **6**(e28154), 1–7.
20 G.-D. Fang, D. D. Dionysiou, S. R. Al-Abed and D.-M. Zhou, Superoxide radical driving the activation of persulfate by magnetite nanoparticles: implications for the degradation of PCBs, *Appl. Catal., B*, 2013, **129**, 325–332.
21 J. R. P. Webster, S. Langridge, R. M. Dalgliesh and T. R. Charlton, Reflectometry techniques on the second target station at ISIS: methods and science, *Eur. Phys. J. Plus*, 2011, **126**, 112.
22 L. G. Parratt, Surface Studies of Solids by Total Reflection of X-rays, *Phys. Rev.*, 1954, **95**, 359–369.
23 B. Efron, Bootstrap methods: Another look at the jackknife, in *Breakthroughs in statistics: Methodology and distribution*,

ed. S. Kotz and N. L. Johnson, Springer New York, New York, NY, 1992, pp. 569–593.
24 A. Nelson, Motofit – integrating neutron reflectometry acquisition, reduction and analysis into one, easy to use, package, *J. Phys.: Conf. Ser.*, 2010, **251**, 012094.
25 A. Nelson, Co-refinement of multiple contrast neutron/X-ray reflectivity data using MOTOFIT, *J. Appl. Crystallogr.*, 2006, **39**, 273–276.
26 F. Heinrich, T. Ng, D. J. Vanderah, P. Shekar, M. Mihailescu, H. Nanda and M. Lösche, A new lipid anchor for sparsely tethered bilayer lipid membranes, *Langmuir*, 2009, **25**, 4219–4229.
27 M. Kosmulski, pH-dependent surface charging and points of zero charge: III. Update, *J. Colloid Interface Sci.*, 2006, **298**, 730–741.
28 M. Kosmulski, The significance of the difference in the point of zero charge between rutile and anatase, *Adv. Colloid Interface Sci.*, 2002, **99**, 255–264.
29 (*a*) F. E. Yakin, M. Barisik and T. Sen, Pore size and porosity dependent z potentials of mesoporous silica nanoparticles, *J. Phys. Chem. C*, 2020, **124**, 19579–19587; (*b*) M. Kokunesoski, J. Gulikovski, B. Matovic, M. Logar, S. K. Milonjic and B. Babic, Synthesis and surface characterization of ordered mesoporous silica SBA-15, *Mater. Chem. Phys.*, 2010, **124**, 1248–1252.
30 F. Collin, Chemical basis of reactive oxygen species reactivity and involvement in neurodegenerative diseases, *Int. J. Mol. Sci.*, 2019, **20**(2407), 1–17.
31 J. Pan, F. A. Heberle, S. Tristram-Nagle, M. Szymanski, M. Koepfinger, J. Katsaras and N. Kučerka, Molecular structures of fluid phase phosphatidylglycerol bilayers as determined by small angle neutron and X-ray scattering, *Biochim. Biophys. Acta, Biomembr.*, 2012, **1818**, 2135–2148.
32 G. Pabst, S. Danner, S. Karmakar, G. Deutsch and V. A. Raghunathan, On the propensity of phosphatidylglycerols to form interdigitated phases, *Biophys. J.*, 2007, **93**, 513–525.
33 N. Kučerka, F. A. Heberle, J. Pan and J. Katsaras, Structural significance of lipid diversity as studied by small angle neutron and X-ray scattering, *Membranes*, 2015, **5**, 454–472.
34 R. Cubitt, T. Saerbeck, R. A. Campbell, R. Barker and P. Gutfreund, An improved algorithm for reducing reflectometry data involving divergent beams or non-flat samples, *J. Appl. Crystallogr.*, 2015, **48**, 2006–2011.
35 A. Erdem, D. Metzler, D. K. Cha and C. P. Huang, The short-term toxic effects of TiO_2 nanoparticles toward bacteria through viability, cellular respiration, and lipid peroxidation, *Environ. Sci. Pollut. Res.*, 2015, **22**, 17917–17924.
36 S. Runa, M. Lakamyali, M. L. Kemp and C. K. Payne, TiO_2 nanoparticle-induced oxidation of the plasma membrane: importance of the protein corona, *J. Phys. Chem. B*, 2017, **121**, 8619–8625.
37 P.-C. Maness, S. Smolinski, D. M. Blake, Z. Huang, E. J. Wolfrum and W. A. Jacoby, Bactericidal activity of photocatalytic TiO_2 reaction: toward an understanding of its killing mechanism, *Appl. Environ. Microbiol.*, 1999, **65**, 4094–4098.
38 J. Kurz, F. Eberle, T. Graumann, M.-E. Kaschler, A. Sähr, F. Neumann, A. H. Dalpke and L. Erdinger, Inactivation of LPS and RNase A on photocatalytically active surfaces, *Chemosphere*, 2011, **84**, 1188–1193.
39 E. Parra-Ortiz, K. L. Browning, L. S. E. Damgaard, R. Nordström, S. Micciulla, S. Bucciarelli and M. Malmsten, Effects of oxidation on the physicochemical properties of polyunsaturated membranes, *J. Colloid Interface Sci.*, 2019, **538**, 404–419.
40 H. Ishiguro, R. Nakano, Y. Yao, J. Kajioka, A. Fujishima, K. Sunada, M. Minoshima, K. Hashimoto and Y. Kubota, Photocatalytic inactivation of bacteriophages by TiO_2-coated glass plates under low-intensity, long-wavelength UV irradiation, *Photochem. Photobiol. Sci.*, 2011, **10**, 1825–1829.
41 F. Collin, Chemical basis of reactive oxygen species reactivity and involvement in neurodegenerative diseases, *Int. J. Mol. Sci.*, 2019, **20**(2407), 1–17.
42 A. A. Dayem, M. K. Hossain, S. B. Lee, K. Kim, S. K. Saha, G.-M. Yang, H. Y. Choi and S.-G. Cho, The role of reactive oxygen species (ROS) in the biological activities of metallic nanoparticles, Int, *J. Mol. Sci.*, 2017, **18**(120), 1–21.
43 X. Lu, X. Feng, J. R. Werber, C. Chu, I. Zucker, J.-H. Kim, C. O. Osuji and M. Elimelech, Enhanced antibacterial activity through the controlled alignment of graphene oxide nanosheets, *Proc. Natl. Acad. Sci. U. S. A.*, 2017, **17109996114**, E9793–E9801.
44 L. Huang, M. Terakawa, T. Zhiyentayev, Y. Y. Huang, Y. Sawayama, A. Jahnke, G. P. Tegos, T. Wharton and M. R. Hamblin, Innovative cationic fullerenes as broad-spectrum light activated antimicrobials, *Nanomedicine*, 2010, **6**, 442–452.
45 D. Y. Lyon and P. J. J. Alvarez, Fullerene water suspension (nC_{60}) exerts antibacterial effects via ROS-independent protein oxidation, *Environ. Sci. Technol.*, 2008, **42**, 8127–8132.
46 C. D. Vecitis, K. R. Zodrow, S. Kang and M. Elimelech, Electronic-structure-dependent bacterial cytotoxicity of single-walled carbon nanotubes, *ACS Nano*, 2012, **4**, 5471–5479.
47 H. Cui, Z. Gu, X. Chen, L. Lin, Z. Wang, X. Dai, Z. Yang, L. Liu, R. Zhou and M. Dong, Stimulating antibacterial activities of graphitic carbon nitride nanosheets with plasma treatment, *Nanoscale*, 2019, **11**, 18416–18425.
48 M. Anpo, G. Costentin, E. Giamello, H. Lauron-Pernot and Z. Sojka, Characterization and reactivity of oxygen species at the surface of metal oxides, *J. Catal.*, 2021, **393**, 259–280.
49 E. Proksch, pH in nature, humans, and skin, *J. Dermatol.*, 2018, **45**, 1044–1052.

